Journal of Applied Fluid Mechanics, Vol. 18, No. 10, pp. 2641-2658, 2025.
Available online at www.jafmonline.net, ISSN 1735-3572, EISSN 1735-3645.
https://doi.org/10.47176/jafm.18.10.3352

Numerical Investigation on the Aerodynamic Performance of Vertical Axis Wind Turbine with the Half-airfoil Wind Collector

Y. Xiao[1], Z. Ye[1,2†], Y. Wang[1,2], C. Li[1,2] and H. Yu[1]

[1] *School of Energy and Power Engineering, University of Shanghai for Science and Technology 1, Shanghai, 200093, China*
[2] *Shanghai Key Laboratory of Multiphase Flow and Heat Transfer in Power Engineering 2, Shanghai, 200093, China*

†*Corresponding Author Email:* yezhou_usst@usst.edu.cn

ABSTRACT

In an effort to boost the aerodynamic performance of vertical axis wind turbines (VAWT), a half-airfoil wind collector structure is proposed, inspired by the contour shape of NACA airfoils. To explore the influence of the half-airfoil wind collector on the performance of VAWTs, an optimization design of the half-airfoil wind collector structure is conducted using the Design of Experiments (DOE) method. Based on the NACA0021 airfoil, simulations of computational fluid dynamics (CFD) are used to examine the instantaneous torque, power coefficient, overall torque, and dynamic flow field of the VAWT blades under the influence of the half-airfoil wind collector. The findings reveal that the half-airfoil wind collector has a good wind-collecting effect, effectively guiding the airflow to concentrate on the blades, increasing the local airflow velocity over the blades, and strengthening the differential in pressure between the blades' inner and outer surfaces. This results in an increased torque on the blades and lessens losses related to the enlargement and detachment of dynamic stall vortices. Consequently, the power coefficient of the VAWT is augmented within the scope of high tip - speed ratio. Specifically, When the tip-speed ratio is 3.08, with geometric parameters of $x = 0$, $d = 29c$, $\alpha = 5°$, and the NACA0021 contour, the highest power coefficient reaches 0.59, showing an improvement of 55.8% over the standard VAWT. When the tip-speed ratio rises, the half-airfoil wind collector maintains a high power coefficient and torque coefficient, demonstrating that it enables the VAWT to operate more efficiently at higher rotational speeds, thus expanding the operational range.

Article History

Received January 3, 2025
Revised April 27, 2025
Accepted May 11, 2025
Available online August 5, 2025

Keywords:

Computational fluid dynamics
Vertical axis wind turbines
Flow control
Wind flow concentration
Aerodynamic characteristics

1. INTRODUCTION

The development and utilization of clean energy is key measures to address global climate change. Wind energy, as a green and renewable energy source, not only lessens the emissions of greenhouse gas but also offers a green solution for global energy supply. It plays a significant role in the worldwide energy transition. (Zoghi et al., 2024). Wind turbines, as the core devices for wind energy conversion, are primarily separated into two categories: Vertical Axis Wind Turbines (VAWT) and Horizontal Axis Wind Turbines（HAWT）. HAWTs are currently the most common wind power generation equipment, widely used because of their high efficiency and mature technology, yet they need wind direction adjustment to maximize energy capture (Abed et al., 2024; Song et al., 2024). In contrast, VAWTs, due to their unique structure, are not restricted by wind direction changes and have broad application potential in areas with unstable wind speeds (Lee et al., 2024). With continuous technological progress, the complementary advantages of both types of wind turbines in different environments will offer more diverse solutions for the wide-spread adoption of clean energy and efficient wind energy utilization.

To enhance the wind energy utilization efficiency of VAWT, flow control techniques are commonly employed around their blades to mitigate flow separation. The two general types of these flow control techniques are Active Flow Control (AFC) and Passive Flow Control (PFC). (Zhang et al., 2023). Active flow control modifies the flow characteristics through external energy input. Typical techniques include blowing (Liu et al., 2022a),

NOMENCLATURE

A	the area swept by the wind turbine blades	R	rotor radius
C_m	moment coefficient	TSR/λ	Tip Speed Ratio
C_p	power coefficient	V_∞	wind speed
C_{pre}	pressure coefficient	VAWT	Vertical Axis Wind Turbines
c	chord line	x	the horizontal distance from the maximum thickness position to the turbine's center of rotation
d	the spacing between the wind collectors	α	the deflection angle between the collector's chord line and the horizontal direction
H	blade height	θ	rotation angle
HAWC	Half-Airfoil Wind Collector	μ	dynamic viscosity
HAWT	Horizontal Axis Wind Turbine	v	kinematic viscosity
M	moment	ρ	density
P	power	ω	angular velocity

jetting (Sun & Huang, 2023), deflecting flaps (Attie et al., 2022), blade deformation (Tong & Wang, 2021), pitch profile and oscillatory pitch program (Rasekh et al., 2023; Rasekh & Aliabadi, 2023), among others, to suppress flow separation. For example, Karimian and Rasekh (2021) investigated the instantaneous torque coefficients across diverse pitch angle and tip speed ratio scenarios, meticulously exploring how pitch angles influence operational dynamics. Results demonstrated that at the optimal *TSR*, a -1° pitch angle configuration yielded a 4.2% enhancement in the C_p. Gupta et al. (2024) focused on optimizing the aerodynamic behavior of VAWTs by applying active pitch control. A high-fidelity CFD simulation was employed to implement adjustable pitch dynamics, targeting both the suppression of low-speed flow stagnation in small turbines and the improvement of C_p across a range of *TSRs*. An improvement of 81% in the C_p was observed when the *TSR* reached 1.5. Additionally, modifying the rotor by employing more blades or utilizing blades with longer chords contributed to minimizing the stagnation area, with the maximum torque achieved using a variable pitch mechanism for 3 and 4-blade rotors. Moreover, Zhu et al. (2019) applied jet control technologies, including blowing, synthetic, and plasma jet actuators, to VAWTs. Despite their potential, jet control strategies require further development to reduce energy and material consumption. Through numerical simulations, they demonstrated that an upward parabolic blowing jet control strategy could effectively suppress flow separation and improve aerodynamic performance, while reducing actuator energy consumption.

Passive flow control, on the other hand, influences the flow by altering the geometric shape of the airfoil. Common techniques include wind collector plates (Li et al., 2023), wing slots (Rainone et al., 2023), flaps (Han et al., 2023), serrations (Liu et al., 2022b), and tubercles (Joseph et al., 2024), among others. For instance, Ahnn et al. (2024) employed biomimetic flaps inspired by bird wing feathers to improve the performance of a simplified VAWT. There was an 88% improvement in the power coefficient at a tip speed ratio (*TSR*) of 0.8 when the flap was placed 0.1c downstream of the blade leading edge. Although the blade's torque remained unaltered, the flap generated additional torque, thereby boosting the overall performance. The flap's motion enabled it to interact with vortices shed from the blade, according to phase analysis. Even in the presence of the flap, the torque of the blade itself stays the same, yet the flap independently generates additional torque on its own, consequently increasing the overall power coefficient.

Active flow control technology requires external energy sources for actuation, such as gas injection or electrical input. This results in additional energy consumption of the system, especially during large-scale applications. In contrast, passive flow control technology does not rely on external energy input, thus the energy consumption of the system itself is very low. In a relatively stable flow environment, passive control can effectively modify the flow characteristics. With the progress advancement of technology, breakthroughs have been achieved in passive flow control technology. To tackle the problem of low wind energy utilization efficiency of vertical axis wind turbines (VAWTs) in complex wind field environments and improve the overall performance of VAWTs, researchers have developed various external auxiliary devices based on passive flow control technology, such as various wind concentrating devices (Zhou et al., 2024), vortex generators (Ivanković et al., 2024), among others. These auxiliary devices can alter the streamline of the wind field, boost the wind energy capture efficiency, and optimize the operating state of the blades. They have become one of the key technologies for enhancing the power coefficient and operating efficiency of VAWTs.

Researchers are committed to the in-depth research, development, and optimization of auxiliary devices for VAWTs, aiming to increase wind energy utilization efficiency. Ghafoorian et al (2024) developed the semi-directional airfoil guide vane (SDAGV) to boost the Savonius VAWT's efficiency and aerodynamic performance. According to the findings, the power coefficient (C_p) can rise by 140% relative to a single Savonius rotor when the guide vane is positioned lower downstream of the rotor. Li et al. (2019) proposed an arc-shaped wind-gathering device (WGD) for straight-blade VAWTs. The device, designed using B-Spline

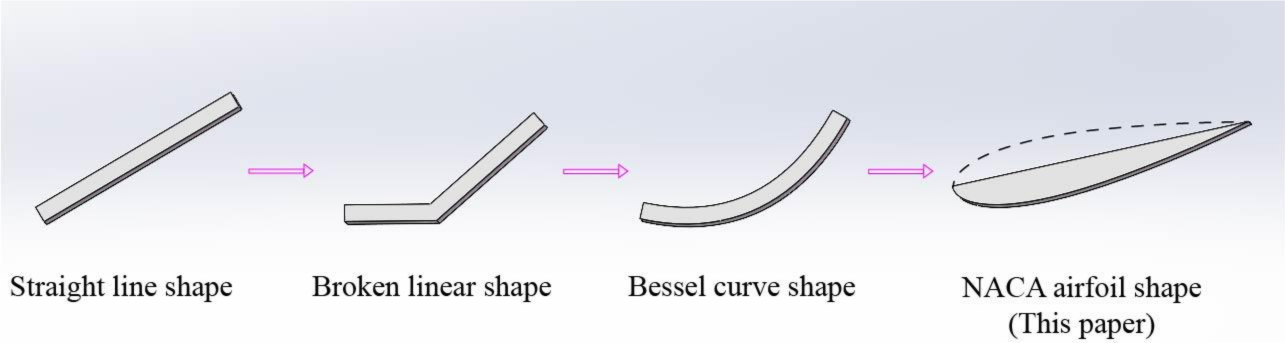

Fig. 1 Different profile shapes of the wind- collector

curves, significantly improved both static and dynamic performance, particularly under low wind speed conditions, with the maximum starting torque increased by 14.8%. Dadamoussa et al. (2020) enhanced the performance of Darrieus wind turbines by introducing a vortex generator (VG) and studying its impact on the turbine's performance. The effects of geometric parameters, such as the VG's size and placement relative to the airfoil, were analyzed. The study showed that optimizing the VG's size and position could significantly improve the turbine's performance, with a small VG height notably increasing the tangential coefficient. Ramesh and Selvaraj (2023) developed four different wind turbine designs: a bare turbine, a diffuser design with a single rotor, a curved diffuser with additional components, and the I^2NS^2F design. The findings indicate that when the inlet wind speed is 5.5 m/s, the I^2NS^2F design attains a wind speed of 53 m/s in the turbine area. This design enhances the natural wind flow, leading to increased power generation. Kuang et al. (2021) designed a closed arc-shaped diffuser to improve the power performance of VAWTs at medium and high TSRs. Through advanced simulations, they studied how diffuser parameters (such as projection length and diffusion angle) affected performance. The results indicated significant power improvements, especially at high TSRs. Farzadi et al (2024) added a baffle to the J-shaped blade VAWT to improve performance by reducing vortex leakage. Positioning the baffle at the blade tip minimized tip vortices and increased the pressure difference, boosting torque. At TSRs of 0.5, 0.75, and 1, torque increased by 49.5%, 38.2%, and 28%, respectively, when compared to the NACA 0021 turbine. Overall, the baffle led to a 17.5% average increase in torque.

The above research reveals that the auxiliary wind-gathering devices significantly enhance the wind energy utilization efficiency and power coefficient of VAWTs. Especially, the shape of the wind-collecting device is considered a key factor affecting its wind-collecting performance. Figure 1 depicts wind collectors with different profiles. Therefore, owing to the excellent aerodynamic characteristics, simple parametric design, and wide adaptability of NACA airfoils, as well as their established design methods and aerodynamic stability under various operating conditions, NACA airfoils are commonly used as the foundational airfoil type in wind turbine designs. Their application in wind-collecting devices has both theoretical and practical value. As such, this paper proposes a Half-Airfoil Wind Collector (HAWC) structure with a NACA airfoil profile, which has promising potential in enhancing the aerodynamic performance and wind energy utilization efficiency of VAWTs.

This study commences by validating the aerodynamic performance of the normal airfoil and VAWT, ensuring the accuracy of the numerical simulation outcomes. Under the same Reynolds number, the numerical simulation results, when compared to the power coefficients from experimental studies, exhibit only small discrepancies, thereby validating the effectiveness of the numerical simulation method. Subsequently, an orthogonal experimental design (DOE) approach is utilized to optimize the design parameters of the Half-Airfoil Wind Collector (Pluszka et al., 2022), with a well-organized experimental procedure enables the identification of the optimal parameter combination, laying the groundwork for further research. Finally, to evaluate the aerodynamic performance of the Half-Airfoil Wind Collector on the VAWT, numerical simulations are performed, confirming the effectiveness of this structure in improving turbine performance. The results indicate that the Half-Airfoil Wind Collector significantly boosts wind energy capture and power coefficient, improves the aerodynamic performance of the turbine, and extends its operational range.

2. PHYSICAL MODELS AND NUMERICAL SIMULATION METHODS

2.1 Geometric Model

A NACA0021-type VAWT was chosen as the subject of this study. The extensive simulation and experimental data gathered from prior research on this type of wind turbine provided an important reference basis for this research (Azadani & Saleh, 2022). The specific parameters of the NACA0021-type VAWT are presented in Table 1.

The Half-Airfoil Wind Collector structure is modeled for the VAWT, as shown in Fig. 2(a). The Half-Airfoil Wind Collector is created by cutting the NACA 0021 airfoil along its chord line, with the maximum thickness (δ_{max}) located at 30% of the cord

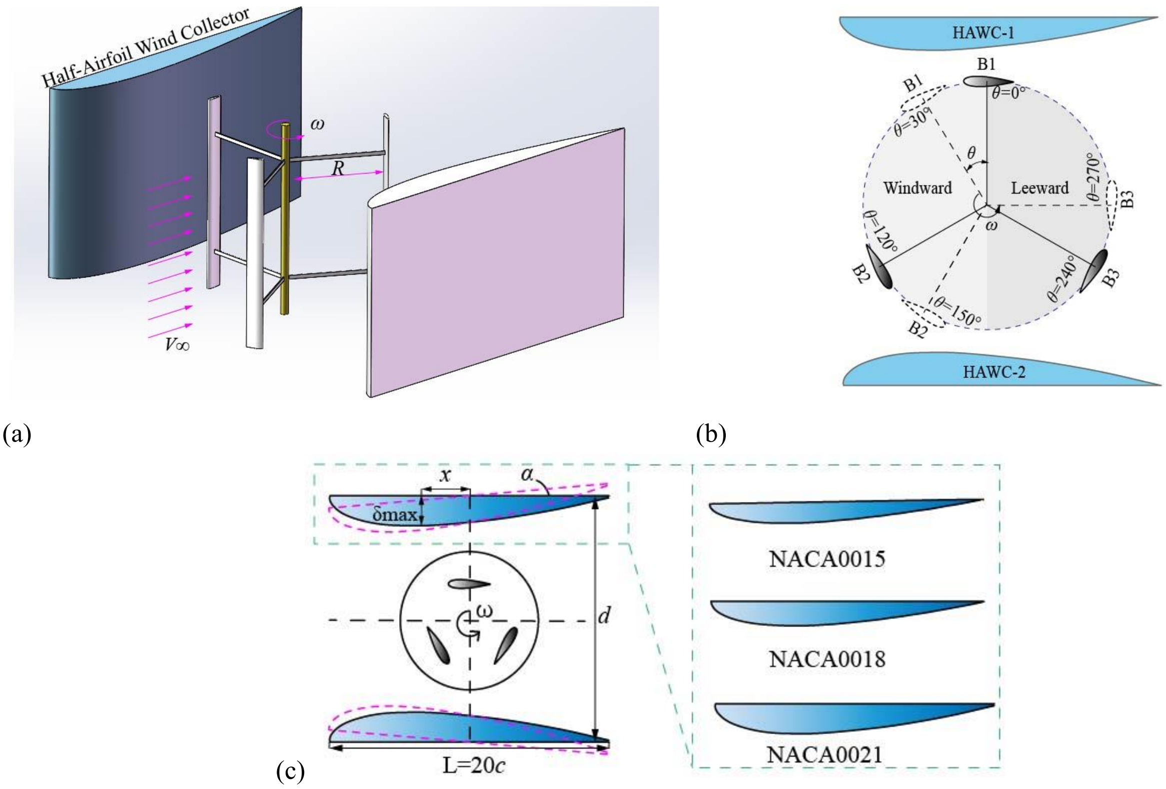

Fig. 2 Schematic diagram of VAWT with the half-airfoil wind collector structure and related airfoils: (a) Three-dimensional schematic of VAWT with the half-airfoil wind collector structure;(b) Two-dimensional top view of VAWT with the half-airfoil wind collector structure;(c) Design parameters of the half-airfoil wind collector structure

Table 1 Parameters of the NACA0021 VAWT

Parameter name	Value	Unit
Number of blades/N	3	-
Chord length/c	0.0858	m
Solidity/σ	0.8	-
Rotor radius/R	0.515	m
Reynolds number	1.067×10^4	-
Blade height/H	1.4564	m
Incoming velocity/V_∞	9	m/s

length from the leading-edge. The chord length (which denotes the direct distance from the leading-edge to the trailing-edge of the airfoil.) of the half-airfoil is 20c, and the VAWT is positioned at the throat of the wind collector. The two-dimensional top view of the VAWT is illustrated in Fig. 2(b), where the rotating domain is divided into the upwind and downwind regions. Figure 2(c) presents the design parameters of the Half-Airfoil Wind Collector vertical axis wind turbine, including the horizontal distance (x) from the maximum thickness position to the turbine's center of rotation, the spacing (d) between the wind collectors, the deflection angle (α) between the collector's chord line and the horizontal direction, and the profile of the wind collector. The Half-Airfoil Wind Collector demonstrates excellent wind-collecting effects, effectively enhancing the flow velocity in the wind turbine's operational region while reducing the extent of the low-velocity wake. As a result, the pressure differential between the inner and outer blade surfaces increases, thereby improving the blade's torque coefficient and wind energy utilization efficiency.

Multiple parameters are involved in the aerodynamic performance evaluation of a VAWT. In addition to indicating the turbine's effectiveness, these elements play a crucial role in its structural design and enhancement. The aerodynamic metrics analyzed in this study include:

Defined as the ratio of the torque (M) experienced by the blade to the standard torque generated by fluid-induced forces, the moment coefficient (C_m) quantifies the blade's rotational influence. The expression is as follows:

$$C_m = \frac{M}{0.5\rho U_\infty^2 c^2} \tag{1}$$

where M is the torque experienced by the blade, with units of $N{\cdot}m$. ρ, symbolizing the air density, is equivalent to 1.18415 kg/m^3; U_∞, indicating the incoming velocity, is equivalent to 9 m/s.

λ, known as the tip speed ratio, is the quotient of the blade tip velocity and the inflow velocity. It is important for optimizing the design of the VAWT, as it affects lift, drag, and moment coefficients. The expression is:

$$\lambda = \frac{\omega R}{U_\infty} \tag{2}$$

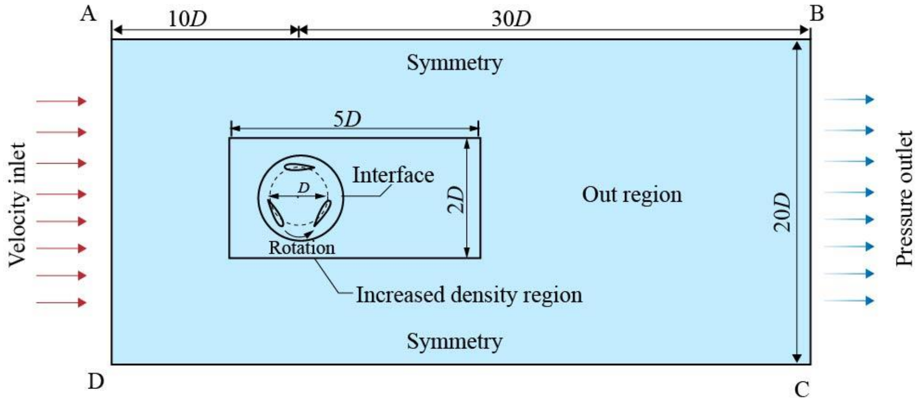

Fig. 3 Calculation domain and boundary conditions of the airfoil

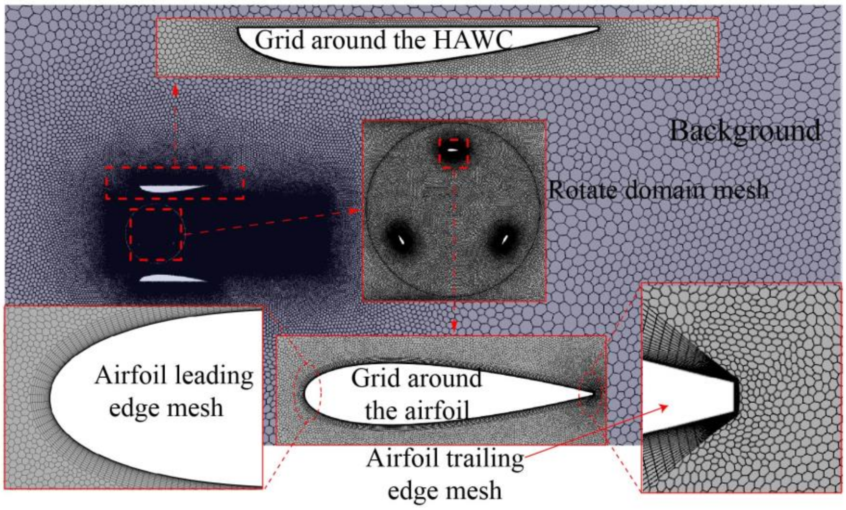

Fig. 4 Compute domain grid

where ω is the rotational speed of the wind turbine, in units of rad/s.

The power coefficient (C_p) is one of the most important performance indicators. This ratio quantifies the efficiency of the turbine by comparing its actual power output to the theoretical wind power within the blade-swept region. The corresponding expression is given as follows:

$$C_p = \frac{P}{0.5\rho A U_\infty^3} \tag{3}$$

Where A represents the area swept by the wind turbine blades, which refers to the area of the circular or approximately circular region swept by the rotating components (such as blades) of the wind turbine during the rotation process. in square meters (m^2).

2.2 Computational Domain and Meshing

To obtain accurate results, it is essential to appropriately discretize the computational domain (Xu et al., 2024). This study employs STAR-CCM+ software for numerical simulations. Figure 3 illustrates the domain partitioning and boundary conditions. The computational domain's inlet is located 10D upstream from the turbine's center of rotation, and the outlet is located 30D away. The computational domain's upper and lower boundaries are designated as symmetry boundaries, with a domain width of 20D. The AD side of the domain serves as the velocity inlet, where the velocity of 9 m/s, while the BC side is set as a pressure outlet. The computational domain consists of three subregions: the external flow region, the mesh refinement zone, and the rotating domain. An interface boundary is set between the external flow region and the rotating domain to ensure proper information exchange between the regions. To capture the flow field more clearly, a mesh refinement zone with a length of 5D and a width of 2D is placed outside the rotating domain to better track the fluid motion in the wake. Throughout the study, air is modeled as an incompressible fluid with a constant density (ρ = 1.18415 kg/m³).

A polyhedral mesh generator is employed in the computational domain to create a two-dimensional polygonal mesh. The mesh distribution and local mesh details are depicted in Fig. 4. Both the internal and external sides of the airfoil and wind collector are equipped with boundary layer meshes. In order to precisely resolve the boundary layer flow, the mesh height of the first layer is configured to 5×10^{-5}m, and

Table 2 Three different computational domain configurations

Case	Inlet distance(D)	Outlet distance(D)	Lateral boundaries(D)	C_p
Case1	8D	25D	15D	0.3594
Case2	10D	30D	20D	0.3652
Case3	12D	35D	25D	0.3660

the mesh growth rate is within the range of 1 to 1.05. This ensures that the non-dimensional y^+ value near the wall is 1.

2.3 Turbulence Model

This study employs the SIMPLE algorithm based on the finite volume method. This method applies second-order accurate discretization to the momentum equation, turbulent energy, and dissipation rate (Davandeh & Maghrebi, 2023). The URANS model is extensively applied in engineering because of its superior efficiency and accuracy. Given the significant advantages of the *k-omega* SST model for accurately depicting boundary layer flows under reverse pressure gradients and free-stream characteristics, especially near the blade wall (Aboelezz et al., 2022). Consequently, the *k-omega* SST model is chosen as the turbulence model for this study. To ensure that the simulation results correspond to experimental data, the turbulence intensity and viscosity ratio are configured to correspond to the experimental values. Specifically, a turbulence intensity of 1%, a turbulence viscosity ratio of 10, and a residual convergence criterion set at 10^{-6}, the Reynolds number in the simulation is maintained in accordance with the experimental parameters. The computed Reynolds number is approximately 1.53×10^5. The governing equations may be formulated as follows:

$$\frac{\partial}{\partial x_i}(u_i) = 0 \tag{4}$$

$$\rho\frac{\partial}{\partial t}(u_i) + \rho\frac{\partial}{\partial x_j}(u_i u_j) = -\frac{\partial P}{\partial x_i} + \mu\frac{\partial}{\partial x_j}\left(\frac{\partial u_i}{\partial x_j}\right) + \frac{\partial}{\partial x_j}\left(-\rho\overline{u_j' u_i'}\right) \tag{5}$$

where, $-\rho\overline{u_j' u_i'}$ corresponds to the Reynolds stress, u_i signifies the air velocity component, P stands for pressure, and μ indicates the air's the kinematic viscosity.

3. RELIABILITY VERIFICATION

3.1 Computational Domain Independence

To ensure that the chosen computational domain does not introduce boundary effects that could influence the numerical results, an independence study of the computational domain was conducted. This analysis examined the impact of domain size on the simulation results by comparing key aerodynamic parameters under different domain dimensions. This study tested three different computational domain configurations at a *TSR* of 2.63, altering the inlet distance, outlet distance, and lateral boundaries. The tested configurations are summarized in Table 2:

The power coefficient (C_p) was compared under different computational domains. As shown in Fig. 2, the results for Case 2 and Case 3 exhibit negligible differences, indicating that the flow is not constrained by the computational domain boundaries. However, in Case 1, minor variations were observed, suggesting that the domain was not large enough to eliminate boundary effects. Based on these findings, Case 2 (10D inlet, 30D outlet, and 20D lateral boundaries) was selected as the optimal configuration, striking a balance between computational efficiency and accuracy. The results confirm that the chosen computational domain is sufficiently large to prevent artificial constraints on the flow field and ensure reliable numerical predictions.

3.2 Grid Independence

To achieve high-accuracy numerical simulations, it is crucial to ensure appropriate mesh resolution around the airfoil. As a result, grid independence verification emphasizes analyzing the refinement level of this region to enhance the credibility of the computational results (Ershuai et al., 2022). By changing the number of mesh nodes and their growth rate around the airfoil, three different mesh densities with 220,000, 280,000, and 320,000 nodes were established. The first-layer mesh thickness and its growth rate were maintained at a constant value, ensuring that the boundary conditions and computational approach remained unchanged. Numerical simulations of the VAWT were conducted with a *TSR* of 2.63 (Zhang et al., 2024). The simulation results of the 10th rotation cycle were selected for the grid independence verification analysis, as by this stage, the flow field had reached a statistically stable state, thus minimizing the influence of initial transients. The aerodynamic forces and wake characteristics exhibited periodic behavior, making this cycle representative for analysis. Figure 5 depicts the VAWT torque coefficient as a function of phase angle for each mesh density configuration.

During the numerical simulations, it was found that the torque calculation results for a single blade showed significant deviations with 220,000 and 280,000 mesh nodes. When the number of mesh nodes increased to 320,000, a significant reduction in the deviation of the VAWT's average torque coefficient was observed, with a change of just 0.58%, gradually stabilizing. The findings suggest that a higher mesh density has a considerable impact on computational accuracy.

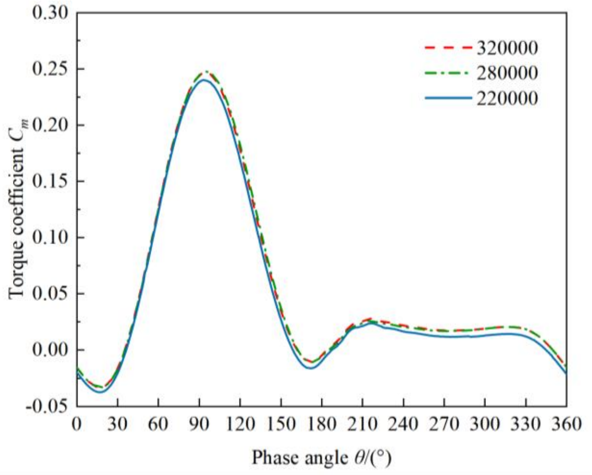

Fig. 5 Grid independence verification

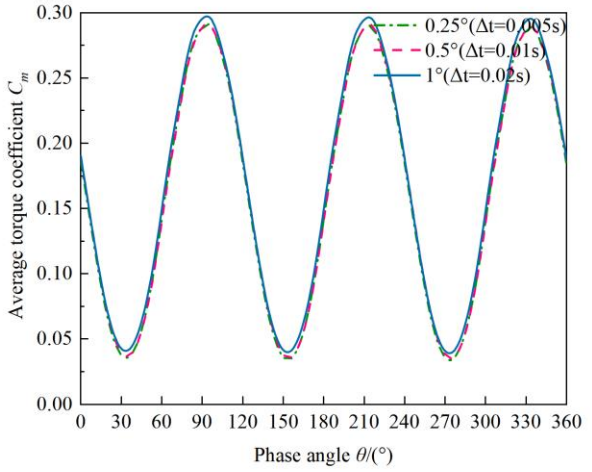

Fig. 6 Time-step independent validation

However, further increasing the mesh density had a limited effect on the torque coefficient of the VAWT. Therefore, to ensure computational accuracy while utilizing computational resources efficiently, 360,000 mesh nodes were selected as the standard for subsequent calculations.

3.3 Time Step Independence

A properly chosen time step is essential for ensuring the precision of the simulation results (Silva & Wolf, 2024). In this study, appropriate time steps were selected and validated, ranging from a time step corresponding to 0.25° to 1° of blade rotation, with the changes in the blade torque coefficient at different time steps shown in Fig. 6. The variation trend is similar to the time step validation results in the literature (Meana et al., 2019). The average torque coefficient varies significantly between the 0.5° and 1° time steps, while the average error in the torque coefficient for the 0.5° and 0.25° time steps is approximately 0.56%. To provide a clearer understanding of the temporal resolution, the time step in seconds (Δt) is determined using the relationship:

$$\Delta t = \Delta\theta/\omega \qquad (6)$$

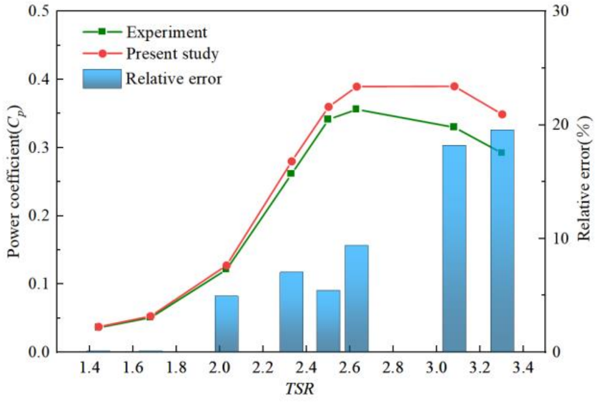

Fig. 7 Comparison of simulation values and experimental values

where Δθ is the time step in degrees, and ω is the rotational speed in degrees per second. Based on this, the time steps of 0.25°, 0.5°, and 1° correspond to time intervals of 0.005s, 0.01s and 0.02s, respectively.

The torque coefficient variation trends are in good agreement with the numerical values, and both 0.5° and 0.25° time steps meet the accuracy requirements. To improve computational efficiency, a 0.5° time step was chosen for subsequent calculations.

3.4 Experimental and Computational Values

To ensure the consistency of the research results with real-world operating conditions, a comparison was made between the numerical simulation results and wind tunnel experimental results (Torres et al., 2022). The average power coefficients obtained from both methods are presented in Fig. 7. At lower *TSR*, the numerical simulation results closely correspond to the experimental data. At elevated TSRs, the computed results exhibited a minor deviation, surpassing the experimental observations. This discrepancy can be attributed to two main factors: First, the two-dimensional model does not take into account three-dimensional effects such as blade tip losses (Maani et al., 2024). In contrast, the experimental data are obtained from three-dimensional measurements, which include mechanical losses caused by the wind turbine main shaft, support rods, and blade tip losses. Second, the influence of three-dimensional turbulence anisotropy on the flow field may also lead to deviations. Despite this, the variation in the average power coefficient from the simulation closely matched the experimental data. The numerical and experimental results exhibited a relative error that did not exceed 20%, fluctuating between a minimum of 3% and a peak of 19%, which confirms that the numerical simulation results are both reasonable and reliable.

4. RESULTS AND ANALYSIS

4.1 Orthogonal Experimental Design

As a structured experimental methodology, the Orthogonal Experimental Design leverages orthogonal

Table 3 Orthogonal test design factors and levels

x	*d*	*α*	Airfoil contour
0	25*c*	1°	NACA0015
2*c*	27*c*	3°	NACA0018
4*c*	29*c*	5°	NACA0021

arrays to systematically plan and arrange experiments, allowing for the efficient analysis of multiple factors and their interactions with a reduced number of trials. Its core concept is to boost experimental efficiency and data representativeness through uniformly distributed and mutually uncorrelated test combinations, thereby reducing experimental costs while ensuring reliable statistical analysis results. In this study, four factors were considered: the horizontal distance of the maximum thickness position from the wind turbine's rotation center (*x*), the spacing between the concentrators (*d*), the deflection angle of the concentrator's chord line relative to the horizontal direction (*α*), and the profile shape of the concentrators. For each factor, three different levels were chosen, resulting in 9 experiments in total as specified by the orthogonal table L9 (4^3). The levels of the factors are as follows: For x, the values of 0, 2*c*, and 4*c* were used; For *d*, the values of 25*c*, 27*c*, and 29*c* were selected; For α, the values of 1°, 3°, and 5° were chosen; For the profile shape of the concentrator, the NACA0015, NACA0018, and NACA0021 airfoils were selected.

This experimental design enables the assessment of the impact of each factor as well as their interactions on the VAWT, while minimizing the number of experiments required. The results are analyzed using range analysis to identify the most influential parameters, thereby ultimately determining the optimal configuration for enhanced wind energy capture efficiency.

ΔC_p is the increase in the wind energy utilization efficiency of the VAWT before and after the installation of the Half-Airfoil Wind Collector. ΔC_p is selected as the evaluation index. The ΔC_p values for each orthogonal experimental design was calculated. As shown in Table 4, adding the Half-Airfoil Wind Collector enhances the C_p of the wind turbine; however, in some cases, the increase in C_p is not significant. This is because the flow field changes caused by the installation of the Half-Airfoil Wind Collector, which interact with the changes in the flow field during the turbine's rotation, resulting in the turbine not reaching a stable state. To further analyze the impact of each factor level on the evaluation index, Table 5 provides the average values and ranges of the indices.

Table 4 Orthogonal test design and results

Case	*x*	*d*	*α*	Airfoil contour	C_p	ΔC_p
1	0	25*c*	1°	NACA0015	0.430	0.040
2	0	27*c*	3°	NACA0018	0.514	0.124
3	0	29*c*	5°	NACA0021	0.592	0.202
4	2*c*	25*c*	3°	NACA0021	0.537	0.147
5	2*c*	27*c*	5°	NACA0015	0.527	0.137
6	2*c*	29*c*	1°	NACA0018	0.458	0.068
7	4*c*	25*c*	5°	NACA0018	0.534	0.144
8	4*c*	27*c*	1°	NACA0021	0.471	0.081

Table 5 Mean and Range of Indicators

Mean *K*	*x*	*d*	*α*	Airfoil contour
K1	1.537	1.502	1.359	1.428
K2	1.521	1.512	1.522	1.506
K3	1.477	1.521	1.654	1.600
$\overline{K1}$	0.512	0.501	0.453	0.476
$\overline{K2}$	0.507	0.504	0.507	0.502
$\overline{K3}$	0.492	0.507	0.551	0.533
Optimal combination	x_1	d_3	α_3	NACA0021
R	0.020	0.007	0.098	0.057

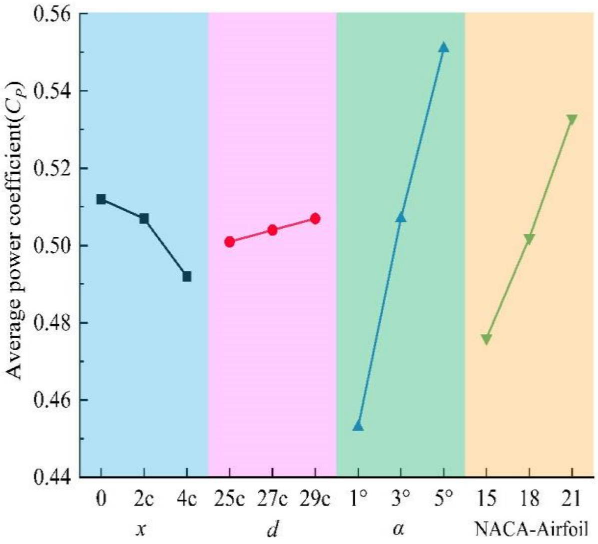

Fig. 8 Average values under different factors and levels

In orthogonal experimental design, the larger the range, a wider range suggests a more substantial effect of the factor on the assessment index. To more intuitively illustrate the degree of influence of each factor, the factors are taken as the horizontal coordinates, and the evaluation index C_p as the vertical coordinate. This gives the relationship between the C_p of the VAWT and the variations of *x*, *d*, *α*, and the airfoil profile, as shown in Fig. 8. The factor α has a significant impact on the reference index, followed by the airfoil profile, while *x* and *d* have a smaller influence. The optimal combination is found to be $x_1d_3\alpha_3$ with the NACA0021 airfoil profile. Therefore, this combination will be employed in subsequent studies.

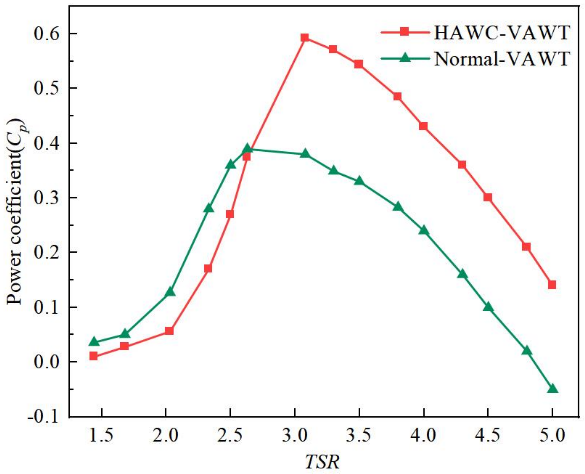

Fig. 9 Power coefficient variation curve with TSR

4.2 Power Coefficient and Torque Coefficient

With reference to the outcomes of the previous orthogonal experiment, the subsequent analysis in this section uses the geometric parameters of the Half-Airfoil Wind Collector: x=0, d=29c, α=5°, and the NACA0021 airfoil profile. The power coefficients within the *TSR* interval of λ=1.44 ~ 5 were calculated and compared with those of the Normal-VAWT. It is apparent from Fig. 9 that, at higher *TSR*, the HAWC-VAWT's C_p significantly increases. Specifically, when λ is 3.08, 3.3, and 3.5, the power coefficients (C_p) of the HAWC-VAWT are 0.59, 0.57, and 0.54, compared to the Normal-VAWT's C_p values (0.38, 0.34, 0.33), representing improvements of 55%, 65%, and 63%. When the *TSR* rises to 4.5, the Normal-VAWT's C_p declines to 0.1, while the HAWC-VAWT still maintains a relatively high C_p value (0.30). The HAWC guides the airflow to concentrate on the blades, increasing the local flow velocity and enhancing the pressure differential across the blade surfaces, thereby delaying the occurrence of flow separation. With the *TSR* rises, the HAWC-VAWT can maintain a high wind energy utilization coefficient, allowing the vertical axis wind turbine to operate more efficiently at higher rotational speeds, thus extending its operational range. However, for TSR values below 3.08, the power coefficient of the HAWC-VAWT is actually lower than that of the normal VAWT. As shown in Fig. 9, in the *TSR* range of approximately 2.0~3.0, the power coefficient of the normal VAWT increases more rapidly, reaching its peak at TSR ≈ 2.63, while the growth of the HAWC-VAWT is relatively slow and does not provide significant improvement. This is because when the blade rotation speed is slow, its tip velocity is too low to effectively drive the surrounding air, resulting in less efficient aerodynamic effects. As a result, the relative wind speed faced by the blades significantly decreases, reducing their ability to capture wind energy. Furthermore, low tip speed ratios may intensify flow disturbances. Although the HAWC is designed to improve wind energy capture, at low tip speed ratios, it may alter the surrounding flow distribution, creating a complex and unstable airflow field. This flow disturbance may lead to more intensified vortex structures and pronounced flow separation, ultimately reducing the wind energy capture efficiency.

To further explore the influence of the HAWC on the VAWT at different phase angles, calculations were performed to determine the system's average torque coefficient for λ=2.03, 2.5, 3.08, and 3.5 as a function of phase angle. Figure 10 presents the obtained results. When the λ=3.08 and 3.5, the C_m of the entire HAWC-VAWT is significantly higher than that of the Normal-VAWT throughout the entire cycle. The largest increase occurs at λ=3.5, with an improvement of 55.9%. However, when the λ is less than 3.08, the performance improvement of the HAWC-VAWT in the windward zone is not significant, and even shows a performance decrease in the leeward zone, leading to an overall torque coefficient lower than that of the Normal-VAWT. This reveals the potential limitations of the Half-Airfoil Wind Collector under low *TSR* conditions.

The variation of the instantaneous torque coefficient with phase angle for a single blade is depicted in Fig. 11, where the HAWC-VAWT and the Normal-VAWT are evaluated at λ = 2.03, 2.5, 3.08, and 3.5. Significant variations in the angle of attack are observed at *TSR*s of 2.03 and 2.5, leading to pronounced fluctuations in torque, especially in the windward region (75° < θ < 135°), where severe flow separation occurs. The torque coefficient of the HAWC-VAWT is reduced by 19.1% and 13.8%, respectively, compared to the Normal-VAWT. The presence of the Half-Airfoil Wind Collector at low tip speed ratios modifies the blade's effective angle of attack by altering its aerodynamic behavior. The lower relative wind speed causes the blade to operate at smaller angles of attack, and the wind deflector causes uneven airflow, leading to some areas of the blade losing the optimal angle of attack, thus reducing the torque coefficient. At *TSRs* of 3.08 and 3.5, the torque significantly increases between 60° and 120°. For the HAWC-VAWT, the torque coefficient increases by 50.7% and 56.2% in comparison to the Normal-VAWT. At elevated *TSRs*, both VAWTs exhibit a nearly identical torque pattern. With the incorporation of the Half-Airfoil Wind Collector, airflow velocity within the turbine increases, promoting a more stable downstream flow field and improving the efficiency.

4.3 Dynamic Flow Field Analysis

Figure 12 illustrates the complete evolution of stall vortices in the Normal-VAWT and the HAWC-VAWT when λ=3.08, including their formation, shedding, and dissipation. The study found that at small azimuth angles, the airflow can easily remain attached to the surface of the reference blade, with no significant flow separation. However, as the azimuth angle increases, the growth of the detached flow region along the suction surface of the reference blade leads to increasingly severe flow separation, particularly at the trailing edge, where large-scale shed vortices appear. These shed vortices not only exacerbate the flow separation on the blade surface but also cause significant interference with downstream blades, leading to a severe imbalance in the flow field,

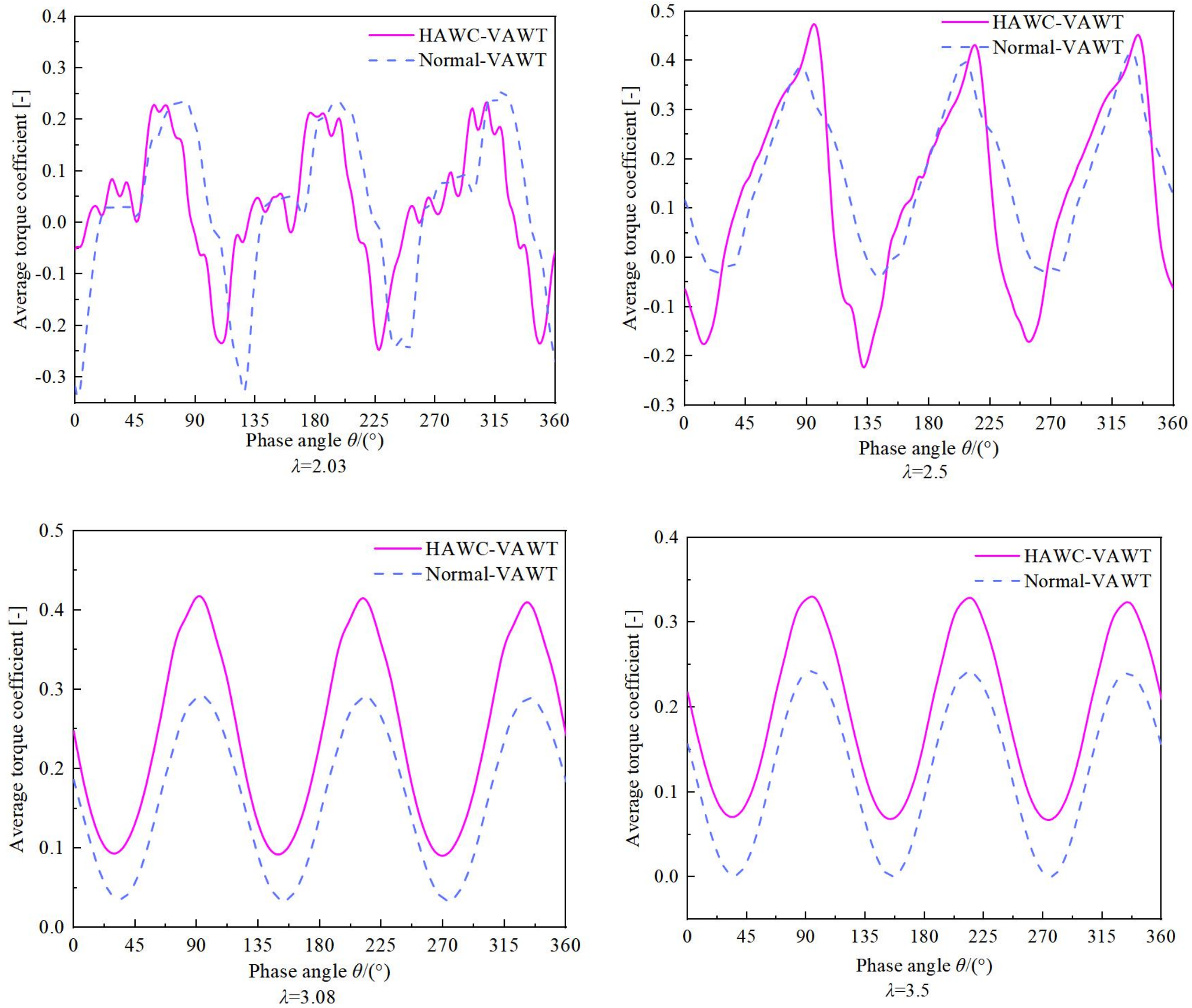

λ=2.03 λ=2.5

λ=3.08 λ=3.5

Fig. 10 Average torque coefficient of HAWC-VAWT and Normal-VAWT for multiple TSRs

which greatly reduces the aerodynamic performance of the VAWT. In contrast, the HAWC structure effectively suppresses the formation of trailing edge shed vortices, reduces the area of the separated flow region, and maintains smooth airflow. Specifically, the HAWC-VAWT blade can effectively slow down the expansion of flow separation, preventing large-scale vortex shedding. Thus, the wind turbine experiences a notable improvement in aerodynamic effectiveness.

At λ=3.08, the HAWC-VAWT reaches its peak power coefficient C_p. To further analyze the improvement in aerodynamic performance brought about by the HAWC structure, we compared the vorticity contours around the blades of the Normal-VAWT and the HAWC-VAWT. In Fig. 13, we specifically selected different phase angles (θ=45°, 90°, 135°, 225°, and 270°) to investigate how the HAWC structure behaves differently in the windward and leeward areas.

According to the analysis, when θ=45°, the airflow smoothly follows the blade contour, with negligible separation, leading to efficient aerodynamic performance. As the azimuth angle increases, at θ=90° and 135°, the Normal-VAWT experiences dynamic stall at the trailing edge, leading to the formation of large separation vortices. These stall vortices enclose a recirculation zone and gradually propagate toward the rear edge of the blade, causing flow instability and severely affecting aerodynamic efficiency. At θ=270°, the normal blade's trailing edge exhibits a more pronounced vortex shedding phenomenon, further exacerbating flow separation. In contrast, the HAWC-VAWT blade shows significant advantages under the same operating conditions. Especially at θ=90°, 135°, and 270°, the trailing edge of the blades of the HAWC structure shows almost no separation vortices, and the flow remains smooth, indicating a strong anti-stall capability. The results suggest that at higher *TSRs*, the HAWC structure plays a crucial role in suppressing flow separation, thereby maintaining more stable aerodynamic performance.

Figure 14 shows the pressure contours surrounding the VAWTs. A detailed analysis of these pressure contours enables an in-depth exploration of the mechanism by which the HAWC structure enhances lift. For conventional airfoils, the vortex structures from the previous cycle significantly affect the blades situated in

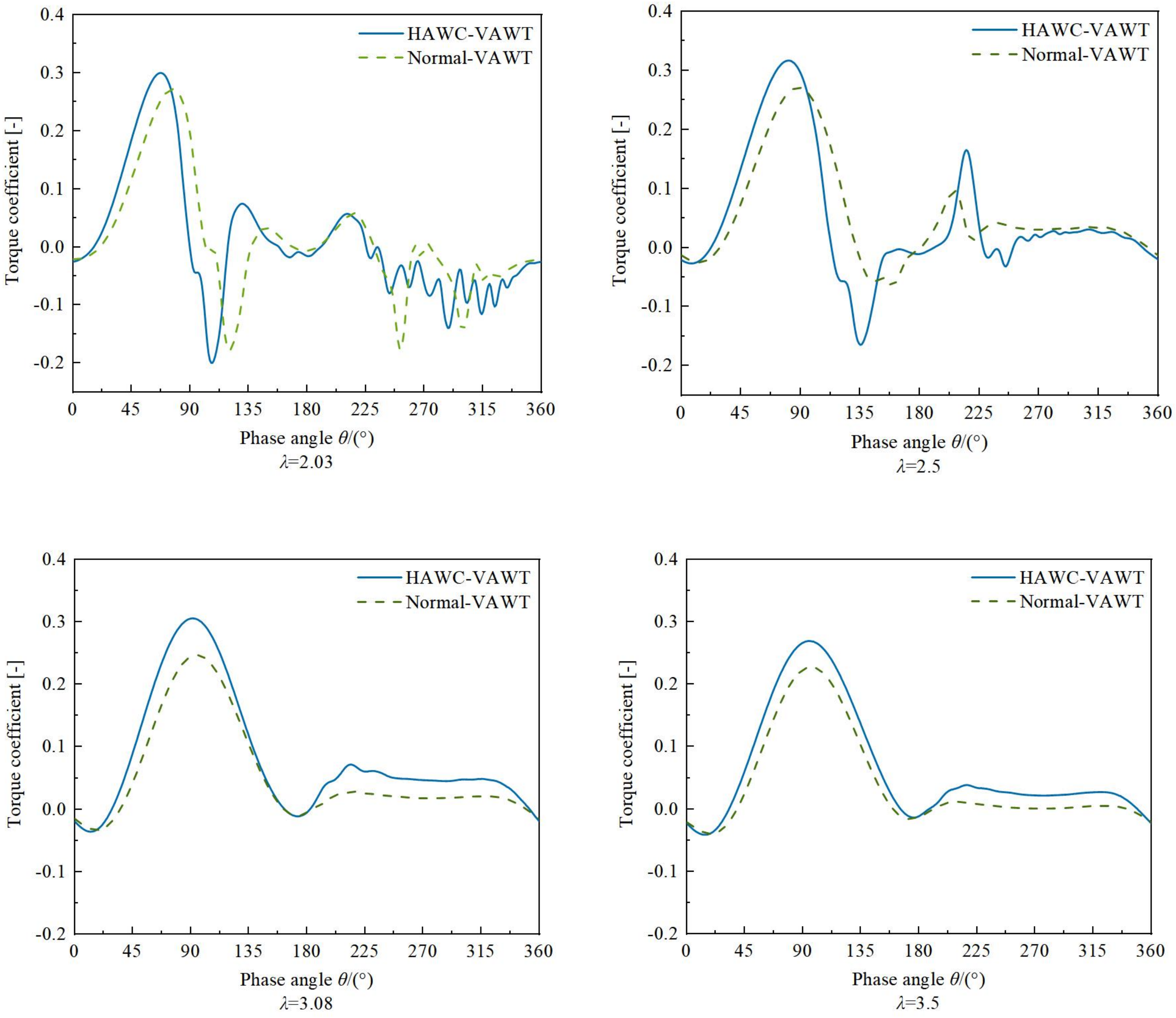

λ=2.03

λ=2.5

λ=3.08

λ=3.5

Fig. 11 Single-blade torque coefficient for HAWC-VAWT and Normal-VAWT with multiple TSRs

the wake area. The instability induced by residual vortices diminishes the pressure differential on the airfoil, leading to a substantial decline in the wind turbine’s aerodynamic performance. Specifically, resulting from flow instability, the pressure difference on the blade surface decreases, boundary layer separation intensifies, and energy loss and lift reduction occur, all of which affect the wind turbine’s overall efficiency.

However, when the HAWC structure is added, this issue is notably alleviated. The HAWC structure effectively increases the pressure disparity between the two sides of the blade. It not only boosts lift but also effectively reduces losses caused by boundary layer fluid separation. Especially at the rear of the airfoil, the effect of inertial and high-speed fluids mixing amplifies turbulent kinetic energy. This amplification of turbulent kinetic energy reduces the negative moment generated at the blade's rear, thus lessening the impact of reverse loads and further improving the wind turbine's operational efficiency and stability.

Figure 15 shows the variation curves of the pressure coefficient at different azimuth angles. When the azimuth angle θ = 45°, the inner boundary layer of the normal airfoil does not experience significant flow separation, and the distribution of the pressure - related coefficient on the side experiencing pressure is similar to that of a conventional airfoil. However, under the same conditions, the HAWC airfoil shows a higher pressure coefficient, suggesting stronger lift generation ability under identical working conditions.

When the azimuth angle θ = 135°, in the back - edge part of the normal airfoil, the boundary layer has significant flow disruption, leading to a sharp drop in the pressure coefficient on the suction surface from 0 to 0.2*c*, which reflects the severe impact of flow separation on aerodynamic performance. In contrast, the HAWC airfoil effectively delays boundary layer separation and maintains a higher suction surface pressure coefficient, enhancing the negative pressure peak and further boosts lift. This phenomenon indicates that the HAWC structure

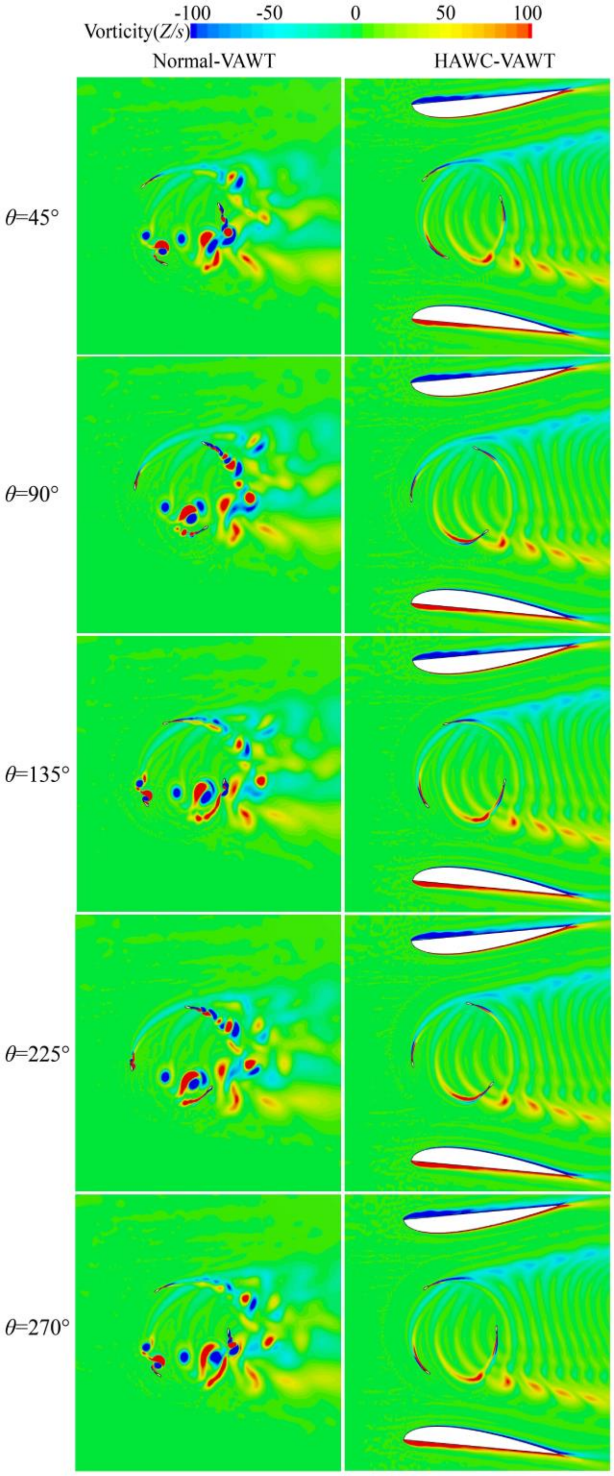

Fig. 12 Comparison of vorticity between HAWC-VAWT and Normal-VAWT at different phase angles

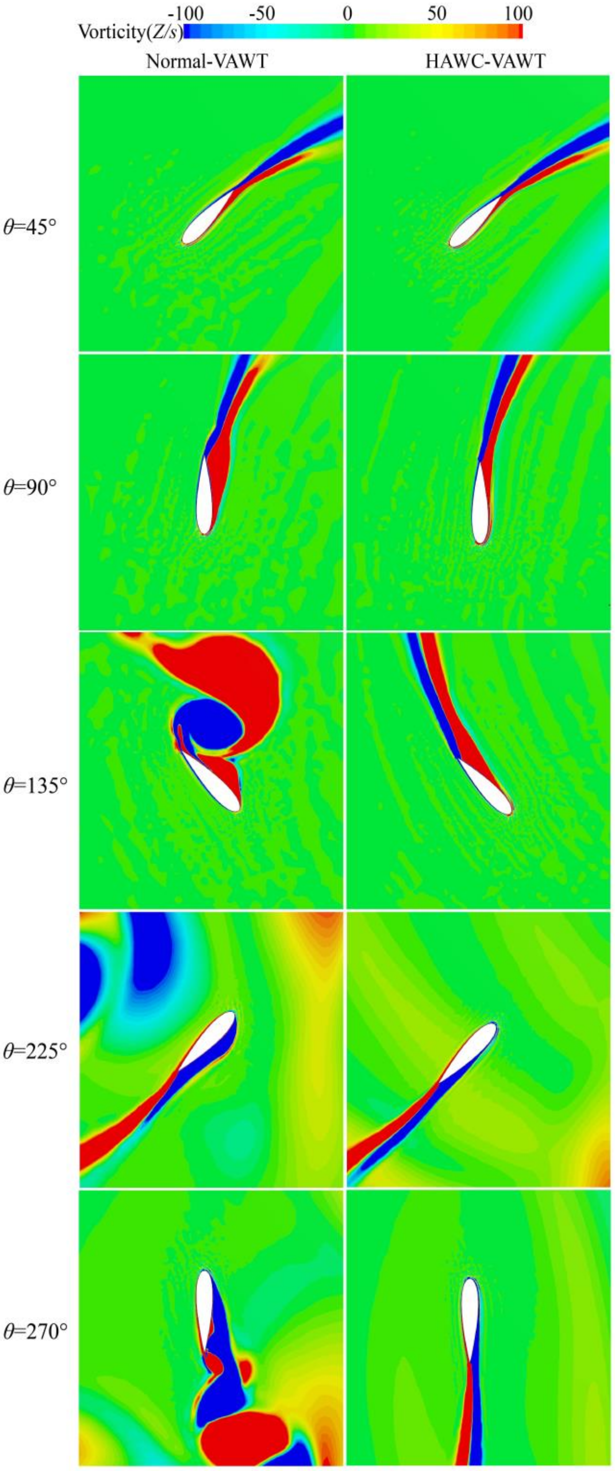

Fig. 13 Comparison of single airfoil vorticity between HAWC-VAWT and Normal-VAWT at different phase angles

can significantly improve the flow stability and the airfoil's aerodynamic properties.

At the point when the azimuth angle θ is 270°, the pressure arrangement at the front tip of the HAWC airfoil is very similar to that of the normal airfoil, suggesting that the influence of the HAWC structure at this azimuth angle is primarily reflected in the flow control at the trailing edge and suction surface. Therefore, although there is little difference at the leading edge, the HAWC structure still improves the overall aerodynamic performance. This improvement enables the HAWC airfoil to maintain higher aerodynamic performance at different azimuth angles, particularly in terms of preventing flow separation, enhancing lift, and reducing energy losses, demonstrating significant advantages.

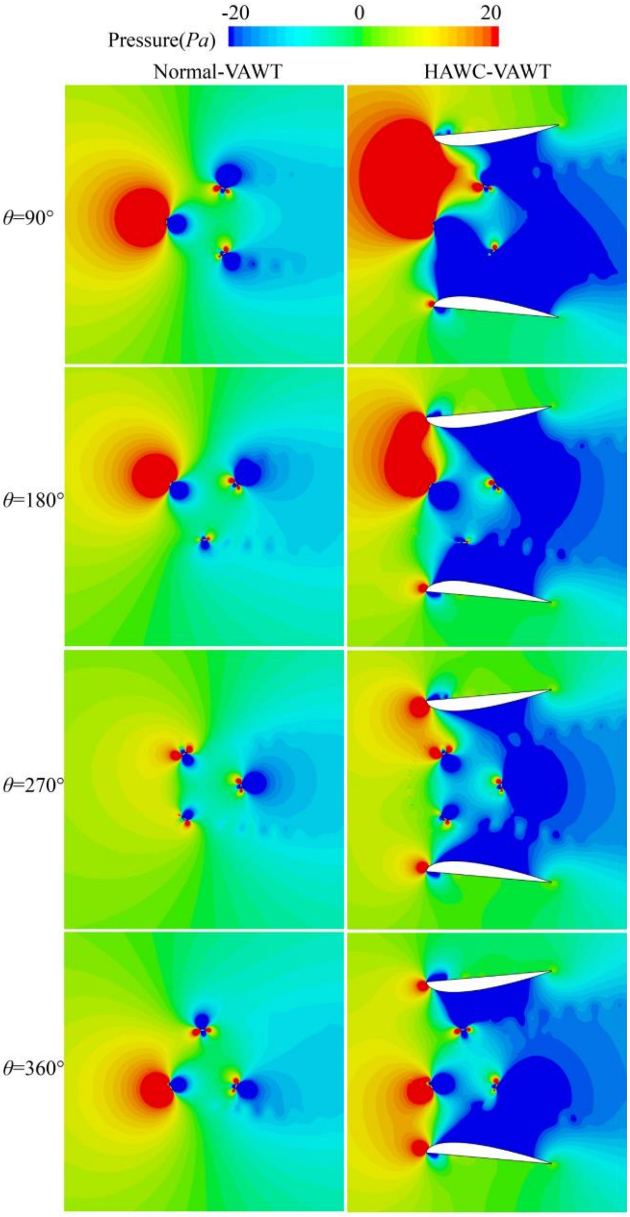

Fig. 14 The impact of HAWC-VAWT and Normal-VAWT pressure distribution

For the purpose of assessing the effect of the HAWC structure on the wake morphology of VAWT, the velocity contour maps of the Normal-VAWT and HAWC-VAWT at *TSR* of 2.03 and 3.08 are contrasted, as depicted in Fig. 16. Based on the analysis of Fig. 16, when the $\lambda = 2.03$, the wake width of the Normal-VAWT is relatively narrow. This situation can be traced back to the quick commingling of the wake flow field and the adjacent free wind. The quick commingling causes the wind speed to quickly recover and leads to increased energy loss. In this case, the wind turbine blades have lower wind energy capture efficiency, and the low-speed region in the wake is more concentrated.

In contrast, the HAWC structure restrains the swift blending of the ambient free air and the wake current field. Effectively, it stops a portion of the free air from penetrating into the wake area. It also alleviates the detachment of the flow on the blade's surface. This allows the blades to harvest wind power more effectively from the oncoming flow. As a result, the breadth of the low - velocity zone in the wake of the HAWC-VAWT is notably wider, manifesting a stronger energy capture ability and a more stable wake structure as opposed to the Normal-VAWT. This finding implies that the HAWC structure exerts two beneficial effects. It improves the aerodynamic characteristics of the wind turbine and optimizes the formation of the wake.

With the *TSR* escalating to 3.08, the HAWC-VAWT's wake width, as opposed to that of the Normal-VAWT, displays a minor increase. For the Normal-VAWT, the wake extends to a length that is about 20 times the blade's radius(20*R*), while the HAWC-VAWT's wake length is decreased to about 18 times the blade radius (18*R*). This indicates that the HAWC structure improves the wake morphology by both expanding the low-speed region to enhance energy capture efficiency and shortening the wake length. Hence, it minimizes the effect on downstream areas and contributes to a further enhancement of the wind turbine's aerodynamic properties.

Figure 17 shows the local flow field velocity streamlines for the Normal-VAWT and HAWC-VAWT. As opposed to the Normal-VAWT, the HAWC structure makes the airflow channel to take on a "front contraction, rear expansion" form, demonstrating good wind convergence performance. It enhances the airflow concentration, accelerates the airflow velocity near the wind turbine, raises the turbulent kinetic power, and as a result, enhances the overall aerodynamic characteristics of the wind turbine.

To gain a more detailed understanding of the velocity characteristics within the wake region generated by the VAWT, velocity data were collected at two distances from the turbine's center of rotation: 4 times the blade radius (4*R*) and 20 times the blade radius (20*R*). The sampling line width was set at 6 times the blade radius (6*R*), and the time-averaged velocity data were normalized based on the velocity magnitude of the free-stream wind. As depicted in Fig. 18, for λ of 2.03, the wake velocity of the HAWC-VAWT is notably lower than of the Normal-VAWT, indicating an increased wake velocity decay. This suggests that the wake takes longer to regain the velocity level of the incoming flow.

Specifically, a minimum dimensionless velocity of 0.33 is observed in the wake of the HAWC-VAWT at $x/R = 4$, which is a decrease of about 9.1% contrasted with the 0.36 value of the Normal-VAWT. This suggests that the HAWC structure, at low *TSR*, is more effective in capturing wind energy and restrains the diffusion of high-speed fluids in the wake region, resulting in a greater reduction in wake velocity. At the downstream location of $x/R = 20$, a gradual recovery in the HAWC-VAWT’s wake velocity is observed, eventually approaching the incoming wind speed, indicating the positive role of the HAWC structure in facilitating the wake recovery process.

However, when λ increases to 3.08, improvements

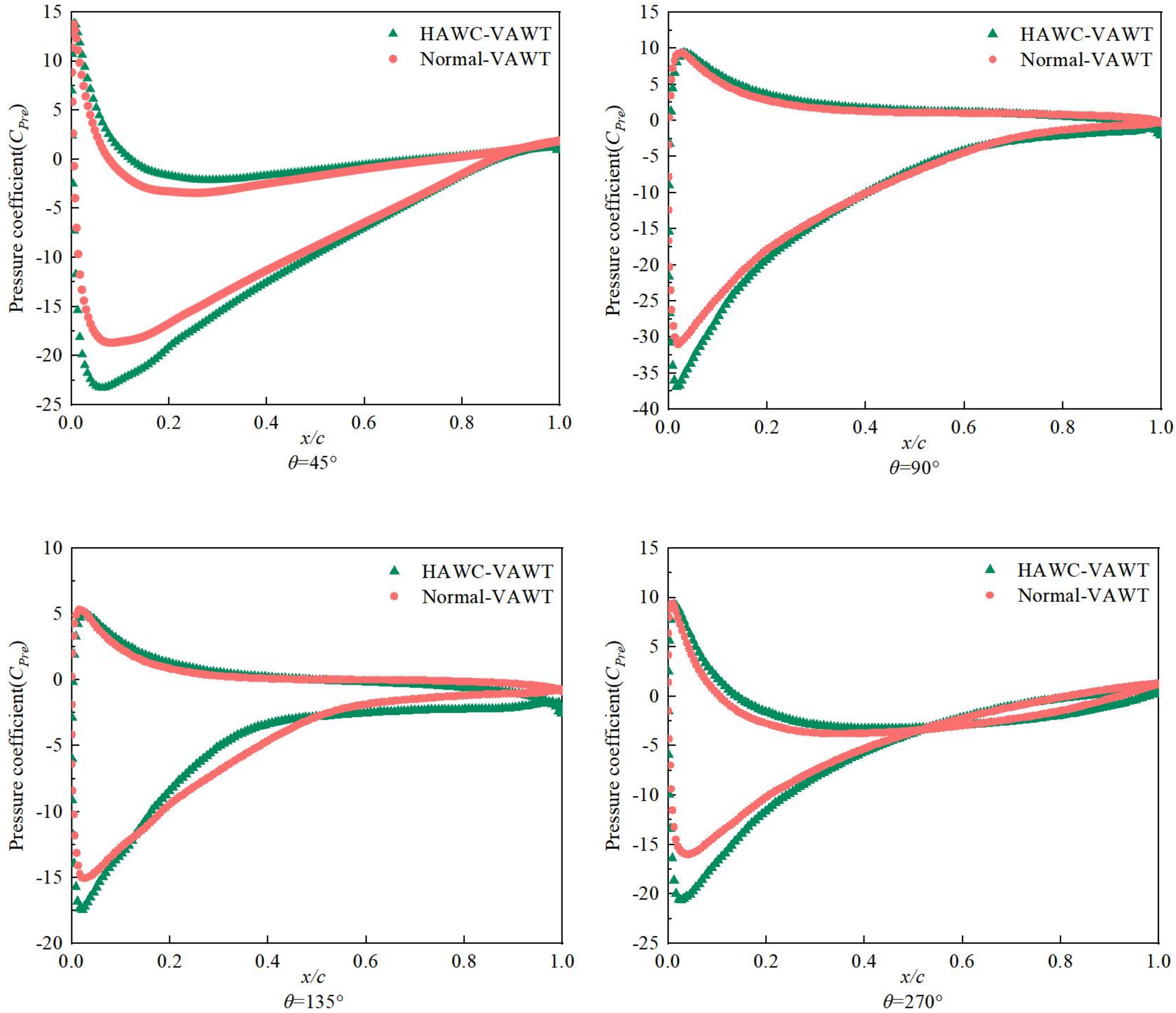

Fig. 15 Comparison of pressure distribution at different phase angles

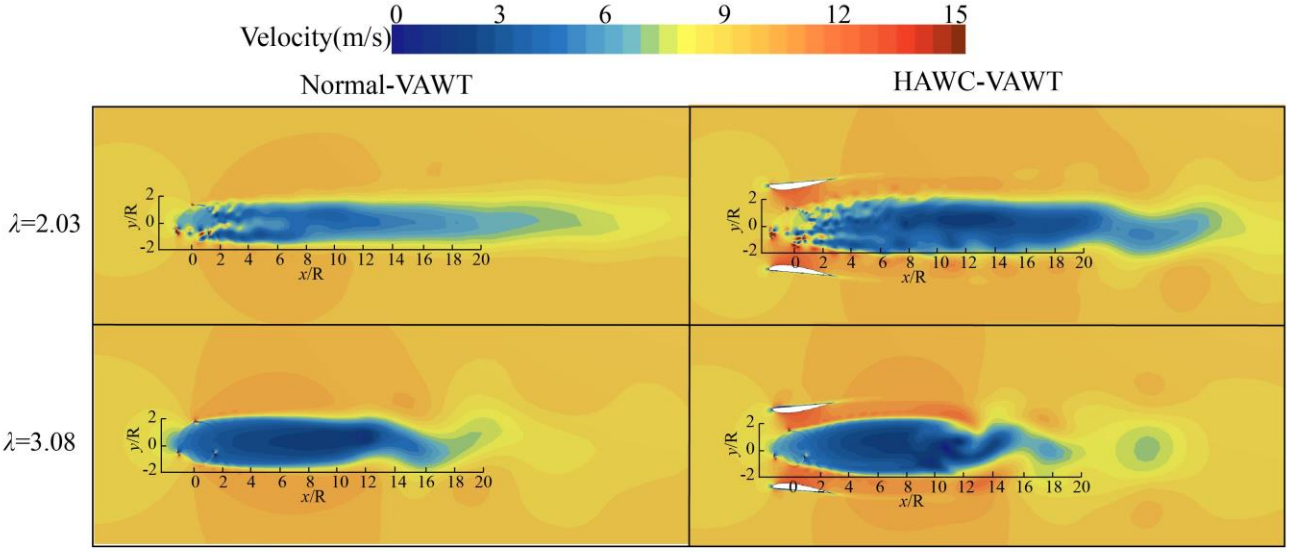

Fig. 16 HAWC-VAWT and Normal-VAWT wake velocity cloud diagram

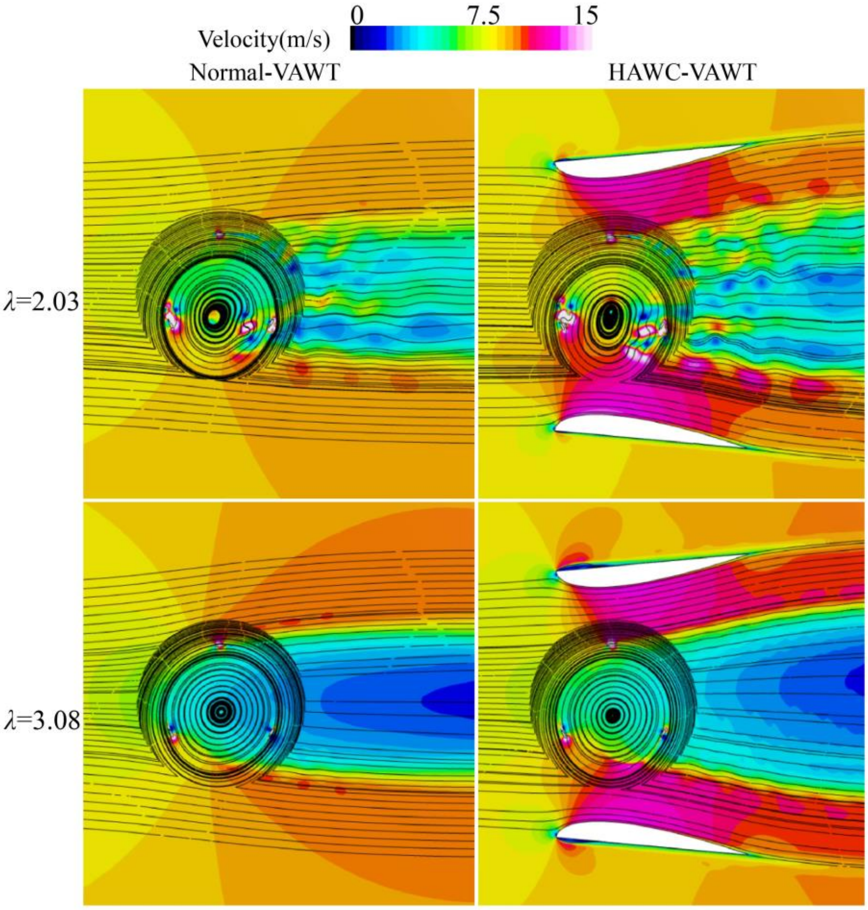

Fig. 17 Velocity streamline cloud map

in aerodynamic performance due to the HAWC structure become limited, and its effect on slowing the wake weakens. It can be inferred that the benefit brought by the HAWC structure tends to decline when the *TSR* becomes higher, and the wake recovery process becomes more similar to that of the Normal-VAWT. When the $x/R = 20$, the wake flow speed shows a gradual return to the upstream wind velocity, suggesting that at higher *TSR*, the wake recovery speed and morphological changes tend towards stabilization.

5. CONCLUSION

This paper proposes a Half-Airfoil Wind Collector structure and applies it to the design of VAWT. The accuracy of the CFD analysis was initially confirmed via computational simulations, and orthogonal experimental design was adopted to optimize the Half-Airfoil Wind Collector structure. The study analyzes how this structure boosts the torque and augments the pressure difference on the blades, and further examines how it influences the aerodynamic performance and unsteady flow characteristics of the VAWT, conducting an in-depth investigation is carried out to reveal the internal mechanisms that contribute to improved wind turbine performance. This research highlights the following key findings:

1. The HAWC airfoil achieves noticeably enhanced aerodynamic efficiency at *TSR* of 3.08 when compared with the normal airfoil. It has an average power coefficient of 0.59, representing an improvement of approximately 55%. Its aerodynamic characteristics are strongly influenced by both the geometric configuration and the angle of deflection. Especially between phase angles of 45° and 135°, where positive torque shows a significant increase. The most significant torque enhancement occurs at a phase angle of 90°.

2. The HAWC structure effectively optimizes the airflow characteristics on the blade, significantly reducing flow separation, which improves the effective lift on the blade and, consequently, the efficiency of wind energy conversion in the VAWT. Notably, at higher *TSR*, the enhancement brought by the HAWC design becomes increasingly evident. Additionally, a substantial increase in the pressure differential across the blade surfaces is observed in the pressure field analysis, which plays a key role in the torque enhancement.

3. The HAWC structure exhibits excellent wind concentration performance, enhancing the flow's convergence, thereby allowing for increased wind energy extraction from the incoming airflow. This design encourages interaction between decelerated fluids at the trailing edge and the surrounding fast-moving streams, increasing the turbulent kinetic energy along the airfoil's exterior, which causes a significant increase in the surface pressure, ultimately enhancing the total performance of the VAWT.

The HAWC structure is of great significance and has

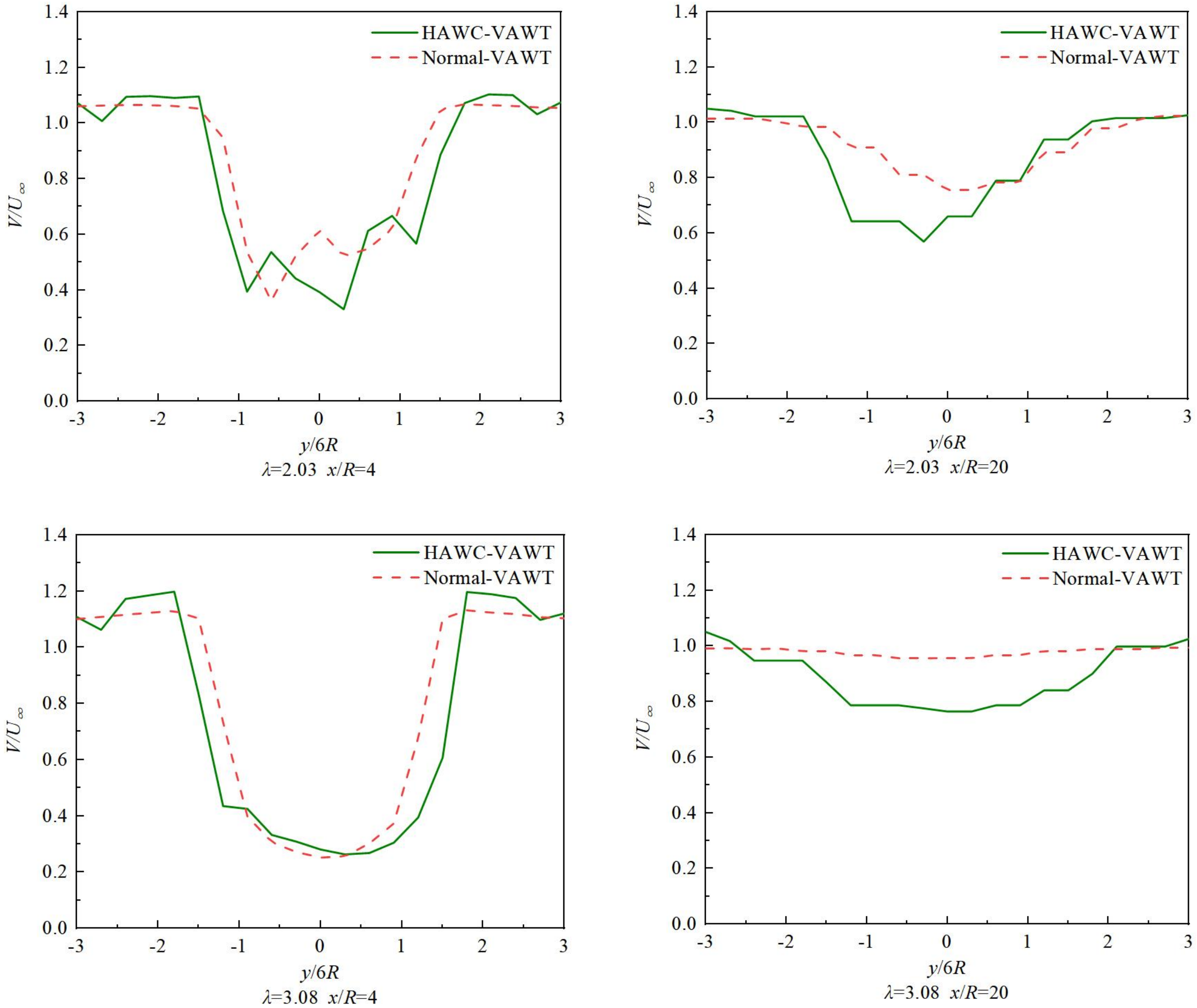

Fig. 18 Dimensionless time-averaged wake velocity changes

broad prospects in the wind power generation field. It optimizes the air flow distribution, enhances the aerodynamic performance of the VAWT, lowers the power generation cost, and provides technical support for the large-scale promotion of wind power generation. Moreover, it provides new ideas for the design of wind turbines. It is anticipated contribute to the research and development of high - efficiency and low - cost wind turbines, and will be widely applied in onshore and offshore wind farms as well as distributed energy systems, facilitating the green transformation of the energy structure and sustainable development.

However, the HAWC might diminish the VAWT's key advantage of not requiring a yaw mechanism. Future research should investigate strategies to balance this trade-off, possibly through innovative designs or control mechanisms. Additionally, the manufacturing complexity of the HAWC, particularly its intricate NACA-inspired curvature, may increase fabrication costs. Despite these challenges, the significant power coefficient improvement enhances energy output, potentially offsetting higher manufacturing and installation costs through a reduced payback period.

ACKNOWLEDGEMENTS

The authors would like to acknowledge the support of Shanghai Pujiang Program (Grant No. 23PJ1409500).

CONFLICT OF INTEREST

The authors declare no competing interests.

AUTHORS CONTRIBUTION

Yi Xiao: Investigation, Writing-Original Draft, Validation; **Zhou Ye :** Supervision, Methodology, Conceptualization, Formal analysis; **Ying Wang:** Writing-Review & Editing, Funding acquisition, Project administration; **Chun Li:** Resources, Investigation; **Hao Yu:** Investigation, Software, Methodology.

REFERENCES

Abed Zahmatkesh Pasand, S., Karimian Aliabadi, S., Ghaemi Osgouie, S. K., & Moshfeghi, M. (2024).

Numerical study of the effect of corona discharge on upward wake flow in the horizontal axis wind turbine farm. *Journal of Applied Fluid Mechanics*, *18*(1), 32-44. https://doi.org/10.47176/jafm.18.1.2547

Aboelezz, A., Ghali, H., Elbayomi, G., & Madboli, M. (2022). A novel VAWT passive flow control numerical and experimental investigations: Guided Vane Airfoil Wind Turbine. *Ocean Engineering*, *257*, 111704. https://doi.org/10.1016/j.oceaneng.2022.111704

Ahnn, S., Kim, H., & Choi, H. (2024). Aerodynamic performance enhancement of a vertical-axis wind turbine by a biomimetic flap. *Bioinspiration & Biomimetics.* https://doi.org/10.1088/1748-3190/ad9a45

Attie, C., ElCheikh, A., Nader, J., & Elkhoury, M. (2022). Performance enhancement of a vertical axis wind turbine using a slotted deflective flap at the trailing edge. *Energy Conversion and Management*, *273*, 116388. https://doi.org/10.1016/j.enconman.2022.116388

Azadani, L. N., & Saleh, M. (2022). Effect of blade aspect ratio on the performance of a pair of vertical axis wind turbines. *Ocean Engineering*, *265*, 112627. https://doi.org/10.1016/j.oceaneng.2022.112627

Dadamoussa, A., Boualem, K., Yahiaoui, T., & Imine, O. (2020). Numerical investigation of flow on a darrieus vertical axis wind turbine blade with vortex generators. *International Journal of Fluid Mechanics Research*, *47*(1), 43–58. https://doi.org/10.1615/interjfluidmechres.2020026791

Davandeh, N., & Maghrebi, M. J. (2023). Leading edge radius effects on VAWT performance. *Journal of Applied Fluid Mechanics*, *16*(9), 1877-1886. https://doi.org/10.47176/jafm.16.09.1626

Ershuai, Q., Wen, X., & Ying, W. (2022). Analysis on the mechanism of different operating conditions for DBD plasma excitation on Savonius VAWT. *Journal of Applied Fluid Mechanics*, *16*(1). https://doi.org/10.47176/jafm.16.01.1377

Farzadi, R., Zanj, A., & Bazargan, M. (2024). Effect of baffles on efficiency of darrieus vertical axis wind turbines equipped with J-type blades. *Energy*, *305*, 132305. https://doi.org/10.1016/j.energy.2024.132305

Ghafoorian, F., Mirmotahari, S. R., & Wan, H. (2024). Numerical study on aerodynamic performance improvement and efficiency enhancement of the savonius vertical axis wind turbine with semi-directional airfoil guide vane. *Ocean Engineering,* *307*, 118186. https://doi.org/10.1016/j.oceaneng.2024.118186

Gupta, A., Abderrahmane, H. A., & Janajreh, I. (2024). Flow analysis and sensitivity study of vertical-axis wind turbine under variable pitching. *Applied Energy*, *358*, 122648. https://doi.org/10.1016/j.apenergy.2024.122648

Han, Z., Chen, H., Chen, Y., Su, J., Zhou, D., Zhu, H., Xia, T., & Tu, J. (2023). Aerodynamic performance optimization of vertical axis wind turbine with straight blades based on synergic control of pitch and flap. *Sustainable Energy Technologies and Assessments*, *57*, 103250. https://doi.org/10.1016/j.seta.2023.103250

Ivanković, M., Manolesos, M., Jentzsch, M., Kozmar, H., & Nayeri, C. N. (2024). Dynamic stall of vertical-axis-wind-turbine rotor blades equipped with Gurney flaps and vortex generators. *Journal of Physics Conference Series*, *2767*(7), 072023. https://doi.org/10.1088/1742-6596/2767/7/072023

Joseph, J., Sridhar, S., A, S., & Radhakrishnan, J. (2024). Analyzing dynamic stall on tubercle mounted VAWT blades: A simplistic experimental approach using an oscillating rig. *Sustainable Energy Technologies and Assessments*, *71*, 103962. https://doi.org/10.1016/j.seta.2024.103962

Ramesh, K, K., & Selvaraj, M. (2023). Investigations on integrated funnel, fan and diffuser augmented unique wind turbine to enhance the wind speed. *Journal of Applied Fluid Mechanics*, *16*(3). https://doi.org/10.47176/jafm.16.03.1498

Karimian, S., & Rasekh, S. (2021). Power and noise performance assessment of a variable pitch vertical axis darrieus type wind turbine. *Journal of the Brazilian Society of Mechanical Sciences and Engineering,* *43*(9). https://doi.org/10.1007/s40430-021-03103-4

Kuang, L., Su, J., Chen, Y., Han, Z., Zhou, D., Zhang, K., Zhao, Y., & Bao, Y. (2021). Wind-capture-accelerate device for performance improvement of vertical-axis wind turbines: External diffuser system. *Energy, 239*, 122196. https://doi.org/10.1016/j.energy.2021.122196

Lee, K., Cruden, A., Ng, J., & Wong, K. (2024). Variable designs of vertical axis wind turbines—a review. *Frontiers in Energy Research*, *12*. https://doi.org/10.3389/fenrg.2024.1437800

Li, Y., Tong, G., Ma, Y., Feng, F., & Tagawa, K. (2023). Numerical study on aerodynamic performance improvement of the straight-bladed vertical axis wind turbine by using wind concentrators. *Renewable Energy*, *219*, 119545. https://doi.org/10.1016/j.renene.2023.119545

Li, Y., Zhao, S., Qu, C., Tong, G., Feng, F., Zhao, B., & Kotaro, T. (2019). Aerodynamic characteristics of Straight-bladed Vertical Axis Wind Turbine with a curved-outline wind gathering device. *Energy Conversion and Management*, *203*, 112249. https://doi.org/10.1016/j.enconman.2019.112249

Liu, Q., Miao, W., Bashir, M., Xu, Z., Yu, N., Luo, S., & Li, C. (2022a). Aerodynamic and aeroacoustic performance assessment of a vertical axis wind turbine by synergistic effect of blowing and suction.

Energy Conversion and Management, *271*, 116289. https://doi.org/10.1016/j.enconman.2022.116289

Liu, K., Song, B., Xue, D., Yang, W., Chen, A., & Wang, Z. (2022b). Numerical study of the aerodynamic effects of bio-inspired leading-edge serrations on a heaving wing at a low Reynolds number. *Aerospace Science and Technology*, *124*, 107529. https://doi.org/10.1016/j.ast.2022.107529

Maani, R. E., Radi, B., & Hami, A. E. (2024). Numerical study and Optimization-Based sensitivity analysis of a Vertical-Axis wind turbine. *Energies, 17*(24), 6300. https://doi.org/10.3390/en17246300

Meana-Fernández, A., Oro, J. M. F., Díaz, K. M. A., & Velarde-Suárez, S. (2019). Turbulence-model comparison for aerodynamic-performance prediction of a typical vertical-axis wind-turbine airfoil. *Energies*, *12*(3), 488. https://doi.org/10.3390/en12030488

Płuszka, P., Malecha, Z., Lewandowski, D., & Surma, K. (2022). Numerical investigation of working fluid properties impacting performance of magnetocaloric cooling device. *Applied Thermal Engineering, 218,* 119305. https://doi.org/10.1016/j.applthermaleng.2022.119305

Rainone, C., De Siero, D., Iuspa, L., Viviani, A., & Pezzella, G. (2023). A numerical procedure for Variable-Pitch law formulation of Vertical-Axis wind turbines. *Energies*, *16*(1), 536. https://doi.org/10.3390/en16010536

Rasekh, S., & Aliabadi, S. K. (2023). Toward improving the performance of a variable pitch vertical axis wind turbine (VP-VAWT), Part 2: Multi-objective optimization using NSGA-II with CFD in the loop. *Ocean Engineering, 278,* 114308. https://doi.org/10.1016/j.oceaneng.2023.114308

Rasekh, S., Aliabadi, S. K., & Hansen, M. O. (2023). Toward improving the performance of a variable pitch vertical axis wind turbine (VP-VAWT), Part 1: Sensitivity analysis using Taguchi-CFD approach. *Ocean Engineering, 279*, 114478. https://doi.org/10.1016/j.oceaneng.2023.114478

Silva, L. J., & Wolf, W. R. (2024). Embedded shear layers in turbulent boundary layers of a NACA0012 airfoil at high angles of attack. *International Journal of Heat and Fluid Flow*, *107*, 109353. https://doi.org/10.1016/j.ijheatfluidflow.2024.109353

Song, M., Moaveni, B., & Hines, E. (2024). Hierarchical Bayesian quantification of aerodynamic effects on an offshore wind turbine under varying environmental and operational conditions. *Mechanical Systems and Signal Processing, 224,* 112174. https://doi.org/10.1016/j.ymssp.2024.112174

Sun, J., & Huang, D. (2023). Impact of trailing edge jet on the performance of a vertical axis wind turbine. *Journal of Mechanical Science and Technology*, *37*(3), 1301–1309. https://doi.org/10.1007/s12206-023-0216-0

Tong, H., & Wang, Y. (2021). Experimental study on unsteady aerodynamic characteristics of deformed blades for vertical axis wind turbine. *Renewable Energy, 173,* 808–826. https://doi.org/10.1016/j.renene.2021.02.139

Torres, S., Marulanda, A., Montoya, M. F., & Hernandez, C. (2022). Geometric design optimization of a Savonius wind turbine. *Energy Conversion and Management*, *262*, 115679. https://doi.org/10.1016/j.enconman.2022.115679

Xu, Z., Dong, X., Li, K., Zhou, Q., & Zhao, Y. (2024). Study of the Self-starting Performance of a Vertical-axis Wind Turbine. *Journal of Applied Fluid Mechanics*, *17*(6), 1261-1276. https://doi.org/10.47176/jafm.17.6.2295

Zhang, Q., Bashir, M., Miao, W., Liu, Q., Li, C., Yue, M., & Wang, P. (2023). Aerodynamic analysis of a novel pitch control strategy and parameter combination for vertical axis wind turbines. *Renewable Energy*, *216*, 119089. https://doi.org/10.1016/j.renene.2023.119089

Zhang, R. Y., Li, D. Y., Wei, X. T., Chang, H., & Wang, H. J. (2024). Blade Airfoil optimization and its impact on vertical axis wind turbine performance. *Journal of Physics Conference Series*, *2854*(1), 012066. https://doi.org/10.1088/1742-6596/2854/1/012066

Zhou, L., Long, Y., Wang, F., Yang, J., Shou, Z., Jia, Q., Sun, F., & Yang, H. (2024). Simulation analysis of wind collecting device for a vertical axis wind turbine. *Journal of Physics Conference Series*, *2736*(1), 012038. https://doi.org/10.1088/1742-6596/2736/1/012038

Zhu, H., Hao, W., Li, C., Ding, Q., & Wu, B. (2019). Application of flow control strategy of blowing, synthetic and plasma jet actuators in vertical axis wind turbines. *Aerospace Science and Technology*, *88*, 468–480. https://doi.org/10.1016/j.ast.2019.03.022

Zoghi, M., Gharaie, S., Hosseinzadeh, N., & Zare, A. (2024). 4E analysis and optimization comparison of solar, biomass, geothermal, and wind power systems for green hydrogen-fueled SOFCs. *Energy, 313,* 133740. https://doi.org/10.1016/j.energy.2024.133740